Journal of Nuclear Medicine, published on July 21, 2010 as doi:10.2967/jnumed.110.076174

^{89}Zr-DFO-J591 for ImmunoPET of Prostate-Specific Membrane Antigen Expression In Vivo

Jason P. Holland[1], Vadim Divilov[1], Neil H. Bander[2,3], Peter M. Smith-Jones[1,4], Steven M. Larson[4–6], and Jason S. Lewis[1,6]

[1]Radiochemistry Service, Department of Radiology, Memorial Sloan-Kettering Cancer Center, New York, New York; [2]Laboratory of Urological Oncology, Department of Urology, New York-Presbyterian Hospital, Weill Medical College of Cornell University, New York, New York; [3]Department of Urology, Memorial Sloan-Kettering Cancer Center, New York, New York; [4]Ludwig Center for Cancer Immunotherapy, Sloan-Kettering Institute, Memorial Sloan-Kettering Cancer Center, New York, New York; [5]Nuclear Medicine Service, Department of Radiology, Memorial Sloan-Kettering Cancer Center, New York, New York; and [6]Program in Molecular Pharmacology and Chemistry, Memorial Sloan-Kettering Cancer Center, New York, New York

^{89}Zr (half-life, 78.41 h) is a positron-emitting radionuclide that displays excellent potential for use in the design and synthesis of radioimmunoconjugates for immunoPET. In the current study, we report the preparation of ^{89}Zr-desferrioxamine B (DFO)-J591, a novel ^{89}Zr-labeled monoclonal antibody (mAb) construct for targeted immunoPET and quantification of prostate-specific membrane antigen (PSMA) expression in vivo. **Methods:** The in vivo behavior of ^{89}Zr-chloride, ^{89}Zr-oxalate, and ^{89}Zr-DFO was studied using PET. High-level computational studies using density functional theory calculations have been used to investigate the electronic structure of ^{89}Zr-DFO and probe the nature of the complex in aqueous conditions. ^{89}Zr-DFO-J591 was characterized both in vitro and in vivo. ImmunoPET in male athymic *nu/nu* mice bearing subcutaneous LNCaP (PSMA-positive) or PC-3 (PSMA-negative) tumors was conducted. The change in ^{89}Zr-DFO-J591 tissue uptake in response to high- and low-specific-activity formulations in the 2 tumor models was measured using acute biodistribution studies and immunoPET. **Results:** The basic characterization of 3 important reagents—^{89}Zr-chloride, ^{89}Zr-oxalate, and the complex ^{89}Zr-DFO—demonstrated that the nature of the ^{89}Zr species dramatically affects the biodistribution and pharmacokinetics. Density functional theory calculations provide a rationale for the observed high in vivo stability of ^{89}Zr-DFO–labeled mAbs and suggest that in aqueous conditions, ^{89}Zr-DFO forms a thermodynamically stable, 8-coordinate complex by coordination of 2 water molecules. ^{89}Zr-DFO-J591 was produced in high radiochemical yield (>77%) and purity (>99%), with a specific activity of 181.7 ± 1.1 MBq/mg (4.91 ± 0.03 mCi/mg). In vitro assays demonstrated that ^{89}Zr-DFO-J591 had an initial immunoreactive fraction of 0.95 ± 0.03 and remained active for up to 7 d. In vivo biodistribution experiments revealed high, target-specific uptake of ^{89}Zr-DFO-J591 in LNCaP tumors after 24, 48, 96, and 144 h (34.4 ± 3.2 percentage injected dose per gram [%ID/g], 38.0 ± 6.2 %ID/g, 40.4 ± 4.8 %ID/g, and 45.8 ± 3.2 %ID/g, respectively). ImmunoPET studies also showed that ^{89}Zr-DFO-J591 provides excellent image contrast, with tumor-to-muscle ratios greater than 20, for the delineation of LNCaP xenografts between 48 and 144 h after administration. **Conclusion:** These studies demonstrate that ^{89}Zr-DFO–labeled mAbs show exceptional promise as radiotracers for immunoPET of human cancers. ^{89}Zr-DFO-J591 displays high tumor–to–background tissue contrast in immunoPET and can be used to delineate and quantify PSMA-positive prostate tumors in vivo.

Key Words: immunoPET; ^{89}Zr; prostate-specific membrane antigen (PSMA); J591; monoclonal antibodies; density functional theory

J Nucl Med 2010; 51:1293–1300
DOI: 10.2967/jnumed.110.076174

The National Cancer Institute estimated that in the United States during 2009, approximately 192,000 cases of prostate cancer (PC) would be diagnosed, with a projected mortality rate of over 27,000 men (>14%). Despite the high incidence of PC, standard diagnostic imaging techniques used for the detection and monitoring of therapy remain inadequate. For example, early-stage, hormonally sensitive tumors on treatment and noncastrate PCs often appear negative on PET scans using either the metabolic radiotracer ^{18}F-FDG or the hormone-based radiopharmaceutical 16β-^{18}F-dihydrotestosterone (^{18}F-FDHT) for imaging the overexpression of androgen receptors (*1*). Therefore, there is an urgent requirement to develop new tools for the noninvasive delineation and staging of PC in vivo.

Prostate-specific membrane antigen (PSMA) is a 100-kDa, type II transmembrane glycoprotein and is one of the best characterized oncogenic markers or targets (*2,3*). PSMA expression has been detected in a limited range of normal tissues including benign prostatic epithelium, renal proximal tubule, small bowel, and brain (a subset of astrocytes). However, these normal sites express PSMA at levels 2–3 orders of magnitude lower than that observed in more

Received Feb. 10, 2010; revision accepted Mar. 30, 2010.
For correspondence or reprints contact: Jason S. Lewis, Radiochemistry Service, Department of Radiology, Memorial Sloan-Kettering Cancer Center, 1275 York Ave., New York, NY 10065.
E-mail: lewisj2@mskcc.org

than 95% of clinical PC specimens (*4,5*). In addition, these normal-tissue PSMA sites are highly polarized to the apical or luminal aspect of the benign prostatic glands, renal tubules and small bowel, basement membrane, and epithelial tight junctions, which form substantial barriers to circulating monoclonal antibodies (mAbs). PSMA expression by astrocytes is similarly sequestered behind the blood–brain barrier. As a result, antibodies to PSMA are functionally tumor-specific, whereas small-molecule PSMA ligands excreted via the renal tubular lumen are not.

PSMA expression levels have been shown to exhibit a positive correlation with increased tumor aggression, metastatic spread, and the development of castrate resistance, or resistance to hormone-based therapies. PSMA expression has also been reported in the neovasculature of most solid tumors (*6*). The failure of ^{18}F-FDG PET for detecting early and treated PC and the acquired resistance of many advanced PCs to androgen-based agents have been the driving force behind recent efforts toward developing novel chemo- and radioimmunoconjugate-based drugs and imaging agents. In particular, in 1996 the U.S. Food and Drug Administration approved the use of ^{111}In-capromab pendetide or ^{111}In-7E11 (^{111}In-ProstaScint; Cytogen Corp.), a murine–mAb specific for an intracellular epitope of PSMA, for SPECT of PC soft-tissue metastases. However, ^{111}In-capromab pendetide for clinical diagnosis is suboptimal because of low sensitivity for viable tumor sites (62% for lymph node metastases, 50% for prostate bed recurrence), which is probably because the number of available targets (presented in dead or dying tissue) is limited. Furthermore, ^{111}In-capromab pendetide does not bind to viable PC sites in bone (the most common site of metastatic disease), and in contrast to PET, SPECT remains only semiquantitative in the clinical setting. Despite these limitations, the National Comprehensive Cancer Network Clinical Practice Guidelines (*5*)—which propose using ^{111}In-capromab pendetide before salvage therapy after radiotherapy or prostatectomy—still recommend the mAb as being useful for specific clinical situations. This fact is testament to the relative lack of better imaging methods for the detection of metastatic prostate cancer, especially in soft tissue.

In 1997, Liu et al. produced 4 mAbs (IgG$_1$: J415, J533, and J591; and IgG$_3$: E99) specific for binding to 2 distinct epitopes on the extracellular domain of PSMA (*7,8*). Subsequent in vitro and in vivo studies identified J591 as the most promising candidate for developing diagnostic and therapeutic immunoconjugates for the targeting of extracellular PSMA in viable tissue (*9–11*). Since these initial studies, J591 has been humanized, and a range of preclinical and clinical studies using J591 radiolabeled with ^{90}Y, ^{177}Lu, or ^{131}I for β-therapy; ^{213}Bi and ^{225}Ac for α-therapy; and ^{111}In for SPECT have been reported (*9–20*).

The work presented here describes the production and preclinical evaluation of ^{89}Zr-radiolabeled humanized-J591 for targeted immunoPET of PSMA-positive tumors in vivo.

MATERIALS AND METHODS

Full details of all methods and equipment used are presented in the supplemental materials (available online only at http://jnm.snmjournals.org).

Density Functional Theory (DFT) Calculations

All calculations were conducted using DFT as implemented in the Gaussian03 suite of ab initio quantum chemistry programs (*21*). Full computational details and Cartesian coordinates of the optimized structures are presented in the supplemental materials. Energetic values are reported in units of kJ mol^{-1}.

Antibody Conjugation and Radiolabeling

The humanized IgG$_1$ mAb J591 was conjugated to the *tris*-hydroxamate hexadentate chelate, desferrioxamine B (DFO) (Calbiochem), using a 6-step procedure modified (*22*) from the approach described by Verel et al. (*23*) (supplemental material).

^{89}Zr was produced via the ^{89}Y(*p*,*n*)^{89}Zr transmutation reaction on a TR19/9 variable-beam-energy cyclotron (Ebco Industries Inc.) in accordance with previously reported methods (*23,24*). The ^{89}Zr-oxalate was isolated in high radionuclidic and radiochemical purity (RCP) greater than 99.9%, with an effective specific activity of 195–497 MBq/μg, (5.28–13.43 mCi/μg) (*24*).

Stability Studies

The stability of ^{89}Zr-DFO-J591 with respect to change in RCP, loss of radioactivity from the mAb, or change in immunoreactivity was investigated in vitro by incubation in solutions of 0.9% saline and 1% bovine serum albumin for 7 d at 37°C. The RCP was determined by radio–instant thin-layer chromatography and γ-counting, and the immunoreactive fraction was measured using the LNCaP cellular binding assay.

Xenograft Models

All animal experiments were conducted in compliance with Institutional Animal Care and Use Committee guidelines. Male athymic *nu/nu* mice (NCRNU-M, 20–22 g, 6–8 wk old) were obtained from Taconic Farms Inc. and were allowed to acclimatize at the Memorial Sloan-Kettering Cancer Center vivarium for 1 wk before tumors were implanted. Mice were provided with food and water ad libitum. In separate animals, LNCaP (PSMA-positive) and PC-3 (PSMA-negative) tumors were induced on the left and right shoulders, respectively. Full details are provided in the supplemental material.

Acute Biodistribution Studies

LNCaP and PC-3 tumor–bearing mice were randomized before the study and were warmed gently with a heat lamp 5 min before administration of ^{89}Zr-DFO-J591 (0.55–0.74 MBq [15–20 μCi], 3–4 μg of mAb, in 200 μL of sterile saline for injection) via injection into the tail vein (0 h). Animals (n = 3–5, per group) were euthanized by CO_2 gas asphyxiation at 24, 48, 96, and 144 h after injection, and 12 organs (including the tumor) were removed, rinsed in water, dried in air for 5 min, weighed, and counted on a γ-counter for accumulation of ^{89}Zr radioactivity. Full details are presented in the supplemental material.

Small-Animal immunoPET

PET experiments were conducted on a microPET Focus 120 scanner (Concorde Microsystems) (*25*). Mice were administered ^{89}Zr-DFO-J591 formulations (10.9–11.3 MBq [295–305 μCi], 60–62 μg of mAb, in 200 μL of 0.9% sterile saline for injection) via injection into the tail vein. Approximately 5 min before PET

images were recorded, mice were anesthetized by inhalation of a 1% isoflurane (Baxter Healthcare)/oxygen gas mixture and placed on the scanner bed. PET images were recorded at various times between 3 and 144 h after injection (supplemental material).

Statistical Analysis

Data were analyzed using the unpaired, 2-tailed Student *t* test. Differences at the 95% confidence level ($P < 0.05$) were considered to be statistically significant.

RESULTS

DFT Calculations

The complexation reaction between ^{89}Zr-chloride or ^{89}Zr-oxalate and the hexadentate, *tris*-hydroxamate chelate [**Fig. 1**] DFO is shown in Figure 1A. Structures of the octahedral complex $[^{89}Zr(HDFO)]^{2+}$ (***1***), the 7-coordinate complexes with *mono*-H_2O coordination in the axial and equatorial sites $[^{89}Zr(HDFO)\text{-ax-}(H_2O)]^{2+}$ (**2-ax**) and $[^{89}Zr(HDFO)\text{-eq-}(H_2O)]^{2+}$ (**2-eq**), and the 8-coordinate complex $[^{89}Zr(HDFO)\text{-}cis\text{-}(H_2O)_2]^{2+}$ (**3-*cis***) were fully optimized using DFT. The optimized structure of the 8-coordinate complex **3-*cis*** is shown in Figure 1B (Supplemental Tables 1–7; Supplemental Figs. 1 and 2).

The calculations revealed that expansion of the coordination sphere to either 7 or 8 coordinates by the addition of 1 or 2 water molecules is thermodynamically favorable. Interestingly, in the 7-coordinate species the axial and equatorial coordination sites, **2-ax** and **2-eq**, are energetically inequivalent. Axial coordination (**2-ax**) is thermodynamically more favorable than equatorial coordination (**2-eq**) by around -41 kJ mol^{-1}. The DFT calculations also suggest that the 8-coordinate complex with *cis*-coordination geometry with respect to the orientation of the H_2O molecules (**3-*cis***) is 95 kJ mol^{-1} more stable than the parent octahedral complex (***1***). Furthermore, complex **3-*cis*** is 14 kJ mol^{-1} more stable than the sum of the thermodynamic stabilization achieved by complexes **2-ax** and **2-eq** (sum = -81 kJ mol^{-1}). This additional stability of complex **3-*cis*** arises because of structural relaxation from the cooperativity of the 2-coordinated H_2O ligands, which allows the $r(Zr\text{-}OH_2(ax))$ to decrease from 0.236 nm in complex **2-ax** to 0.233 nm in complex **3-*cis*** (Supplemental Table 6). Natural bond-order charge analysis (Supplemental Table 7) also supports the conclusion that thermodynamic stabilization of complex **3-*cis*** arises from increased electrostatic interaction between the Zr^{4+} ion and axial H_2O ligand (ligand-to-metal charge transfer). We expect that the coordinated H_2O ligands would be kinetically labile and that species **1–3** were likely in rapid equilibrium at physiologic temperatures.

Basic Characterization of ^{89}Zr Species In Vivo

Before full studies on ^{89}Zr-radiolabeled mAbs are begun, it is important to understand the in vivo behavior of various ^{89}Zr-labeled species, including the starting reagents, and potential impurities or metabolites. Therefore, we examined the biodistribution of ^{89}Zr-chloride and ^{89}Zr-oxalate and the complex ^{89}Zr-DFO using PET (Fig. 2). Maximum-intensity-projection images of ^{89}Zr-chloride and ^{89}Zr-oxalate (11.1 MBq [300 μCi], 200 μL of sterile saline) were recorded at 24 h after injection in the tail vein of male athymic *nu/nu* mice (*24*). ^{89}Zr-chloride was found to be sequestered in the liver, with little excretion (Supplemental Fig. 3). In contrast, administration of ^{89}Zr-oxalate (most likely present as the thermodynamically stable species $[^{89}Zr(C_2O_4)_4]^{4-}$) showed a high accumulation of ^{89}Zr radioactivity in bones, joints, and potentially cartilage (Supplemental Fig. 4). Previous dynamic PET studies on ^{89}Zr-DFO demonstrated that this complex is excreted rapidly within 20 min via a renal pathway, with a measured biologic half-life of 305 ± 6 s (Supplemental Figs. 5 and 6). [**Fig. 2**]

Radiochemistry

J591 was functionalized with DFO using bioconjugation methods modified from the pioneering work of Verel et al. (*23*). The conjugation and purification chemistry was found to proceed in a moderate to high yield (65% ± 5%), with high chemical purity (>95%). Radiolabeling of DFO-J591 with ^{89}Zr-oxalate was achieved at room temperature, in slightly alkaline solutions (pH 7.7–8.1), with crude radiochemical yields (>95%, $n = 6$). Facile purification of ^{89}Zr-DFO-J591 from small-molecule radiolabeled impurities was achieved using either size-exclusion chromatography or spin-column centrifugation. The final

RGB

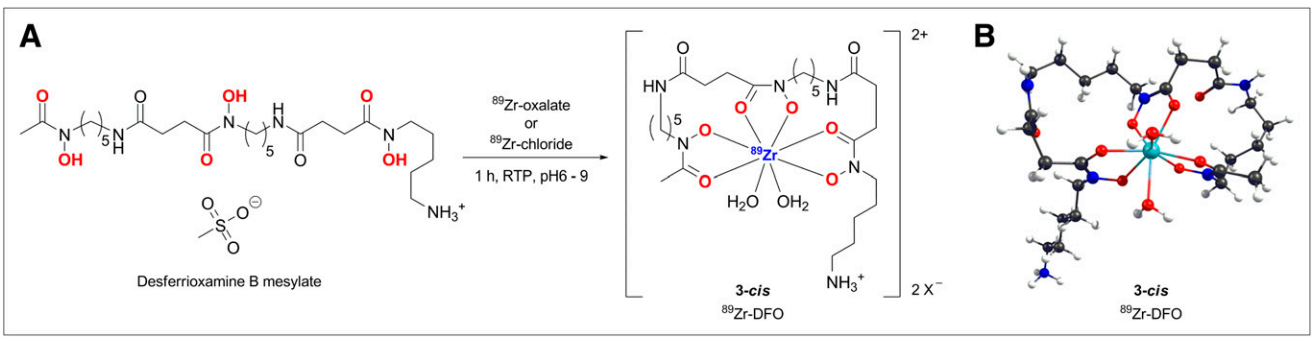

FIGURE 1. (A) Complexation reaction between $[^{89}Zr(C_2O_4)_4]^{4-}$ and DFO. (B) DFT-optimized structure of 8-coordinate complex $[^{89}Zr(HDFO)\text{-}cis\text{-}(H_2O)_2]^{2+}$ (**3-*cis***).

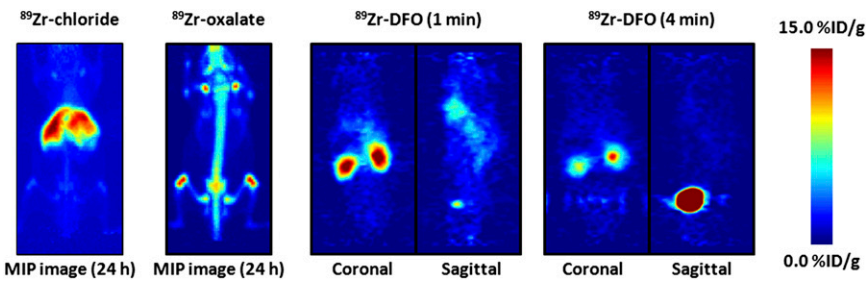

FIGURE 2. PET images showing maximum intensity projection of ^{89}Zr-chloride and ^{89}Zr-oxalate at 24 h after intravenous administration and dynamic PET images of ^{89}Zr-DFO at 1 and 4 min after injection. For maximum-intensity-projection images, upper and lower intensity thresholds were set at 100% and 0%, respectively. Further details are presented in Supplemental Figures 3–6. MIP = maximum intensity projection.

radiochemical yield of the purified ^{89}Zr-DFO-J591 was greater than 77%, and the product was formulated in 0.9% sterile saline with an RCP greater than 99% (n = 6) and a specific activity of 181.7 ± 1.1 MBq/mg (4.91 ± 0.03 mCi/mg) of mAb (Supplemental Figs. 7 and 8). The specific activity obtained in these studies compares favorably with the previously reported specific activities of other ^{89}Zr-radiolabeled mAbs (*22,26–32*). Isotopic dilution assays revealed an average of 3.9 ± 0.3 accessible chelates per mAb.

^{89}Zr-DFO-J591 Immunoreactivity and Stability Studies In Vitro

The immunoreactive fraction of the ^{89}Zr-DFO-J591 formulations was measured by specific in vitro cellular association assays using LNCaP (PSMA-positive) cells before each in vivo experiment (Supplemental Fig. 9) (*33*). In studies using ^{213}Bi-labeled J591, McDevitt et al. reported that the LNCaP cell line had an estimated 180,000 PSMA molecules per cell (*11*). However, in other studies using ^{111}In- and ^{131}I-labeled mAbs (including J415, J533, J591, and 7E11), we found higher PSMA copy numbers (600,000–800,000 sites/cell) for viable LNCaP cells (*9*). The average immunoreactive fraction of ^{89}Zr-DFO-J591 was 0.95 ± 0.03 (n = 4). Control experiments (n = 4) using the PC-3 (PSMA-negative) cell line showed no binding, further demonstrating the specificity of ^{89}Zr-DFO-J591 for PSMA-expressing cells.

Incubation of ^{89}Zr-DFO-J591 in either saline or 1% bovine serum albumin for 7 d at 37°C revealed a less than 2% decrease in RCP (via demetalation), with an observed approximate 17% decrease in the immunoreactive fraction for the 1% bovine serum albumin experiment (0.78 ± 0.03, Supplemental Fig. 10). Therefore, in the absence of specific proteolysis or reductive or oxidative metabolism, ^{89}Zr-DFO-J591 is expected to remain intact and immunoreactive in vivo on a time scale suitable for immunoPET.

Biodistribution Studies

The ability of ^{89}Zr-DFO-J591 to target an extracellular epitope of the PSMA type II transmembrane glycoprotein receptor in vivo was initially assessed by conducting acute biodistribution studies in LNCaP tumor–bearing mice at 24, 48, 96, and 144 h after intravenous administration (Table 1; Supplemental Table 8; Fig. 3). The data reveal that high LNCaP tumor uptake was observed 24 h after injection (34.4 ± 3.2 percentage injected dose per gram [%ID/g]), with a steady increase through 48 (38.0 ± 6.2 %ID/g) and 96 h (40.4 ± 4.8 %ID/g) and reaching 45.8 ± 3.2 %ID/g at 144 h (P = 0.01 between LNCaP uptake at 24 and 144 h). This high accumulation of ^{89}Zr-DFO-J591 is consistent with extraction of the activity from the blood pool (24 h, 21.8 ± 2.8 %ID/g; 48 h, 4.4 ± 1.9 %ID/g; and 96 h, 1.4 ± 0.8 %ID/g) and rapid internalization of the J591–PSMA complex, followed by sequestration of the ^{89}Zr radioactivity inside the cell. In contrast, ^{89}Zr-DFO-J591 uptake in the PC-3 (PSMA-negative) tumors at 48 (15.6 ± 2.1 %ID/g, P = 0.0025) and 96 h (24.0 ± 2.6 %ID/g, P = 0.0017) showed a statistically significant decrease in ^{89}Zr accumulation, compared with uptake in PSMA-positive tumors. ^{89}Zr-DFO-J591 activity in the blood remained 4-fold higher at 48 h (19.0 ± 1.1 %ID/g, P = 0.001) and 10-fold higher at 96 h (13.0 ± 1.8 %ID/g, $P < 0.05$) in mice bearing PC-3 tumors, compared with the corresponding LNCaP tumor–bearing mice (48 h, 4.4 ± 1.9 %ID/g; 96 h, 1.4 ± 0.8 %ID/g).

[**Table 1**] [**Fig. 3**]

Competitive inhibition (blocking) studies using low-specific-activity formulations (60-fold decrease, 3.04 MBq/mg [0.082 mCi/mg]), compared with high-specific-activity formulations, revealed only 10.3 ± 0.8 %ID/g tumor uptake at 48 h after injection, an approximate 4-fold decrease ($P < 0.002$) (Tables 1 and 2; Fig. 3). Furthermore, in the low-specific-activity experiments, ^{89}Zr-DFO-J591 activity in the blood remained high (2- to 3-fold higher at 48 h, 10.7 ± 0.4 %ID/g, P = 0.026), but ^{89}Zr-accumulation in the liver showed a statistically significant decrease from 17.7 ± 1.6 %ID/g to 5.1 ± 0.4 %ID/g ($P < 0.004$). The competitive inhibition experiments concur with the in vitro data and further demonstrate the specificity of ^{89}Zr-DFO-J591 for the PSMA in vivo.

[**Table 2**]

Interestingly, in the LNCaP tumor–bearing mice, ^{89}Zr uptake in the bone was relatively high and increased between 24 and 96 h (24 h, 4.0 ± 0.8 %ID/g; 48 h, 8.2 ± 1.2 %ID/g; and 96 h, 8.7 ± 1.5 %ID/g) before decreasing slightly to 7.4 ± 1.3 %ID/g at 144 h. In contrast, bone accumulation of ^{89}Zr activity in the PC-3 tumor–bearing

TABLE 1. Biodistribution Data of ^{89}Zr-DFO-J591, Administered Intravenously to Mice Bearing Subcutaneous LNCaP Tumors

Organ	24 h (n = 4)	48 h (n = 5)	96 h (n = 5)	144 h (n = 4)	Block (300 μg of mAb) at 48 h (n = 4)
Blood	21.8 ± 2.8	4.4 ± 1.9	1.4 ± 0.8	2.6 ± 1.5	10.7 ± 0.4
Tumor	34.4 ± 3.2	38.0 ± 6.2	40.4 ± 4.8	45.8 ± 3.2	10.3 ± 0.8
Heart	7.4 ± 2.2	4.0 ± 1.3	1.7 ± 0.6	1.4 ± 0.5	3.8 ± 0.7
Lung	11.7 ± 1.9	5.7 ± 3.1	2.2 ± 0.9	2.5 ± 0.9	5.7 ± 0.3
Liver	11.7 ± 1.5	17.7 ± 1.6	17.2 ± 2.7	11.2 ± 1.6	5.1 ± 0.4
Spleen	8.8 ± 4.3	21.1 ± 0.3	24.6 ± 1.8	4.6 ± 2.4	3.1 ± 0.7
Kidney	10.1 ± 1.0	7.5 ± 1.5	5.1 ± 0.5	5.3 ± 0.5	5.1 ± 0.2
Muscle	1.1 ± 0.1	0.6 ± 0.3	0.4 ± 0.4	0.2 ± 0.2	0.8 ± 0.2
Bone	4.0 ± 0.8	8.2 ± 1.2	8.7 ± 1.5	7.4 ± 1.3	2.4 ± 0.3
Tumor/blood	1.6 ± 0.2	8.7 ± 4.1	29.7 ± 17.1	18.0 ± 10.5	1.0 ± 0.1
Tumor/heart	4.7 ± 1.5	9.6 ± 3.5	23.4 ± 9.0	31.9 ± 10.7	2.7 ± 0.5
Tumor/lung	2.9 ± 0.5	6.7 ± 3.7	18.4 ± 7.7	18.5 ± 6.8	1.8 ± 0.2
Tumor/liver	2.9 ± 0.5	2.1 ± 0.4	2.3 ± 0.5	4.1 ± 0.7	2.0 ± 0.2
Tumor/spleen	3.9 ± 1.9	1.8 ± 0.3	1.6 ± 0.2	9.9 ± 5.2	3.3 ± 0.8
Tumor/kidney	3.4 ± 0.5	5.1 ± 1.3	7.9 ± 1.2	8.6 ± 1.1	2.0 ± 0.2
Tumor/muscle	32.4 ± 4.6	59.2 ± 28.8	95.9 ± 95.3	306.4 ± 432.2	13.3 ± 3.1
Tumor/bone	8.7 ± 1.9	4.7 ± 1.0	4.6 ± 1.0	6.2 ± 1.2	4.3 ± 0.6

Complete biodistribution data are presented in Supplemental Table 7. Data are expressed as mean %ID/g ± SD. Errors for tumor-to-tissue ratios are calculated as geometric mean of SD. LNCaP tumors: 3–4 μg mAb; PSMA-positive, 50–250 mm^3.

mice was reduced by approximately 45% at 48 and 96 h (4.3 ± 0.6 %ID/g and 5.1 ± 0.5 %ID/g, respectively).

ImmunoPET with ^{89}Zr-DFO-J591

Temporal immunoPET images of ^{89}Zr-DFO-J591 (10.9–11.3 MBq [295–305 μCi], 60–62 μg of mAb, in sterile saline [200 μL]) recorded in LNCaP and PC-3 tumor–bearing mice between 3 to 144 h are presented in Figure 4. Time–activity curves generated from the immunoPET images showing the mean %ID/g radiotracer uptake in various tissues including the heart and blood pool, liver, and muscle in mice bearing LNCaP (n = 3) or PC-3 (n = 3) tumors are given in Figure 5. Radiotracer uptake in LNCaP tumors was observed less than 24 h after injection of ^{89}Zr-DFO-J591, and high tumor-to-muscle (T/M) ratios (calculated using the mean %ID/g values derived from volume-of-interest analysis of the immunoPET images) were observed. At 48 h after injection, the immunoPET-measured mean and maximum %ID/g for radiotracer uptake in LNCaP tumor–bearing mice was 21.9 ± 0.6 and 38.2 ± 4.9 %ID/g, respectively, with a mean T/M ratio of 15.85 (Supplemental Table 8). By 120 and 144 h, the mean T/M ratio in LNCaP tumors increased to 22.49 and 25.89, respectively. The lower uptake observed in the quantitative immunoPET studies, compared with the biodistribution studies, is likely due to the different total masses of mAb administered (*22*).

[**Fig. 4**]

[**Fig. 5**]

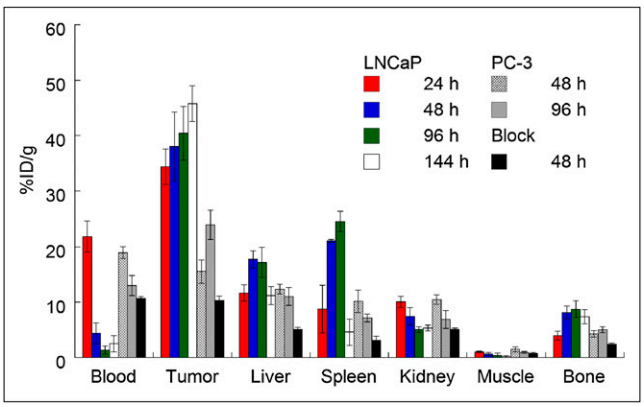

RGB

FIGURE 3. Bar chart showing selected tissue biodistribution data (%ID/g) for uptake of either high- (181.7 ± 1.1 MBq/mg [4.91 ± 0.03 mCi/mg]; 3–4 μg of mAb per mouse) or low-specific-activity (60-fold decrease, 3.04 MBq/mg [0.082 mCi/mg]; 300 μg of mAb per mouse) formulations of ^{89}Zr-DFO-J591 (0.55–0.74 MBq [15–20 μCi], in 200 μL of sterile saline for injection) in male athymic nu/nu mice bearing subcutaneous LNCaP (PSMA-positive) or PC-3 (PSMA-negative) tumors.

In contrast to the high absolute tumor uptake and tumor-to-background contrast ratios observed in the LNCaP model, low accumulation and immunoPET contrast ratios for ^{89}Zr-DFO-J591 uptake in PC-3 (PSMA-negative) tumors (Supplemental Tables 9 and 10; mean T/M ratios of 3.48, 4.36, and 4.19 at 48, 120, and 144 h, respectively) were observed. Uptake in these PC-3 tumors is in accordance with the enhanced permeation and retention mechanism (Supplemental Tables 9 and 10; Supplemental Figs. 11–13).

DISCUSSION

PET has distinct advantages over SPECT in terms of sensitivity and contrast resolution, especially for deep tissues, and these improved imaging characteristics are

TABLE 2. Biodistribution Data of ^{89}Zr-DFO-J591, Administered Intravenously to Mice Bearing Subcutaneous PC-3 Tumors (3–4 μg of mAb)

Organ	48 h (n = 4)	96 h (n = 3)
Blood	19.0 ± 1.1	13.0 ± 1.8
Tumor	15.6 ± 2.1	24.0 ± 2.6
Heart	6.8 ± 0.1	4.3 ± 0.9
Lung	12.6 ± 1.9	7.0 ± 2.3
Liver	12.4 ± 0.9	11.0 ± 1.6
Spleen	10.2 ± 2.0	7.2 ± 0.7
Kidney	10.5 ± 0.9	6.9 ± 1.6
Muscle	1.5 ± 0.4	0.9 ± 0.2
Bone	4.3 ± 0.6	5.1 ± 0.5
Tumor/blood	0.8 ± 0.1	1.8 ± 0.3
Tumor/heart	2.3 ± 0.3	5.6 ± 1.4
Tumor/lung	1.2 ± 0.3	3.4 ± 1.2
Tumor/liver	1.3 ± 0.2	2.2 ± 0.4
Tumor/spleen	1.5 ± 0.4	3.4 ± 0.5
Tumor/kidney	1.5 ± 0.2	3.5 ± 0.9
Tumor/muscle	10.4 ± 3.3	25.4 ± 5.8
Tumor/bone	3.6 ± 0.7	4.7 ± 0.7

Complete biodistribution data are presented in Supplemental Table 7. Data are expressed as mean %ID/g ± SD. Errors for tumor-to-tissue ratios are calculated as geometric mean of SD. PC-3 tumors: PSMA-negative, 70–90 mm^3.

particularly important for radioimmunoimaging. Basic characterization of the in vivo behavior of several important ^{89}Zr-labeled species, including the starting reagents ^{89}Zr-chloride and ^{89}Zr-oxalate and the key complex ^{89}Zr-DFO, are reported. The nature of the aqueous-phase ^{89}Zr species using PET was shown to dramatically affect the in vivo biodistribution, with ^{89}Zr-chloride and ^{89}Zr-oxalate sequestering for over 24 h in the liver and bones, respectively. In contrast, ^{89}Zr-DFO is first-pass excreted through the kidneys and accumulates in the bladder, with a biologic half-life of 305 ± 6 s.

In this work, the novel radiopharmaceutical ^{89}Zr-DFO-J591 has been characterized by a range of stability and cellular association assays in vitro. Previous studies have shown that although diethylenetriaminepentaacetic acid can be used for chelation and radiolabeling of mAbs with $^{89}Zr^{4+}$ ions, demetalation occurs in vivo, and until new ligands are produced DFO remains the chelate of choice (*24,34,35*). Experiments on ^{89}Zr-DFO mAbs have reported high in vivo stability with respect to demetalation or ligand dissociation and relatively low levels of radiotracer accumulation in background tissue in both animals and humans (*26–28,30–32*).

The nature of the electronic structure of the ^{89}Zr–DFO complex has been explored using high-level DFT calculations. The computational results provide a rationale for the high experimentally observed in vitro and in vivo stability of the ^{89}Zr-DFO–labeled radioimmunoconjugates. DFT studies suggest that the origin of the observed in vivo stability of ^{89}Zr-DFO mAbs lies in a combination of the inherently high thermodynamic and kinetic stability of the ^{89}Zr–DFO complex due to strong electrostatic interactions, coupled with the enhancement in thermodynamic stability induced by expansion of the first coordination sphere and geometry relaxation to give an 8-coordinate species. Indeed, in the case of ^{89}Zr-DFO—and in contrast to the more familiar complexes with radionuclides of copper, gallium, indium, and yttrium—these calculations indicate that the presence of water or, for example, coordinating anions such as chloride, may actually increase the thermodynamic stability of the ^{89}Zr–DFO complex in vivo.

The ability of ^{89}Zr-DFO-J591 to target PSMA-expressing tissue was examined using acute biodistribution studies and immunoPET in vivo. The results demonstrate that ^{89}Zr-DFO-J591 shows high specific uptake in LNCaP (PSMA-positive) tumors. Although a direct comparison with earlier work is made difficult because of the use of different models and murine-J591, the absolute tissue uptake values of ^{89}Zr-DFO-J591 (humanized mAb) in most organs at various time points were found to be higher than those observed for either ^{111}In-DOTA-labeled or ^{131}I-labeled J591 (*10*). For example, at 48 h after administration the tumor uptake value was 13.6 ± 2.8 for ^{111}In-DOTA-J591 and 11.2 ± 2.9 %ID/g for ^{131}I-J591, with corresponding blood-pool activities of 8.98 ± 2.10 and 8.57 ± 2.04 %ID/g, respectively. In contrast, tumor uptake and concordant blood-pool activity of ^{89}Zr-DFO-J591 at 48 h were 38.0 ± 6.2 and 4.4 ± 1.9 %ID/g, respectively. As revealed in the biodistribution data, the high immunoreactivity and specificity of ^{89}Zr-DFO-J591 (Tables 1 and 2; Supplemental Table 8) led to a high uptake in the PSMA-positive tumors.

The degree of bone uptake is consistent with previously reported studies using various other ^{89}Zr-labeled mAbs—including ^{89}Zr-DFO-trastuzumab (*22,32*), for imaging *HER2/neu* expression, and ^{89}Zr-DFO-bevacizumab, for imaging vascular endothelial growth factor (*36*). The nature of the radioactive species accumulating in the bone remains uncertain, but it is plausible that slow intratumoral metabolism and subsequent recirculation of ^{89}Zr-labeled metabolites may occur. Full metabolic studies are beyond the scope of the current study and will be the subject of further investigations. However, in a recent clinical trial investigating the radiation dosimetry of ^{89}Zr-DFO-U36 (a chimeric mAb directed against CD44v6) in 20 patients with head and neck squamous cell carcinoma, the liver was identified as the dose-limiting organ (*28,29*). Dosimetry studies based on the biodistribution data presented in this work suggest that for clinical patient studies, kidney uptake of ^{89}Zr-DFO-J591 is the dose-limiting factor.

The immunoPET data demonstrate that ^{89}Zr-DFO-J591 imaging provides high tumor–to–background tissue ratios and that this high uptake is specific for PSMA expression in tissue. Overall, the novel radiotracer ^{89}Zr-DFO-J591 represents a promising candidate for translation to the clinic as an immunoPET agent for the noninvasive delineation of PSMA-positive primary and metastatic prostate cancers in vivo.

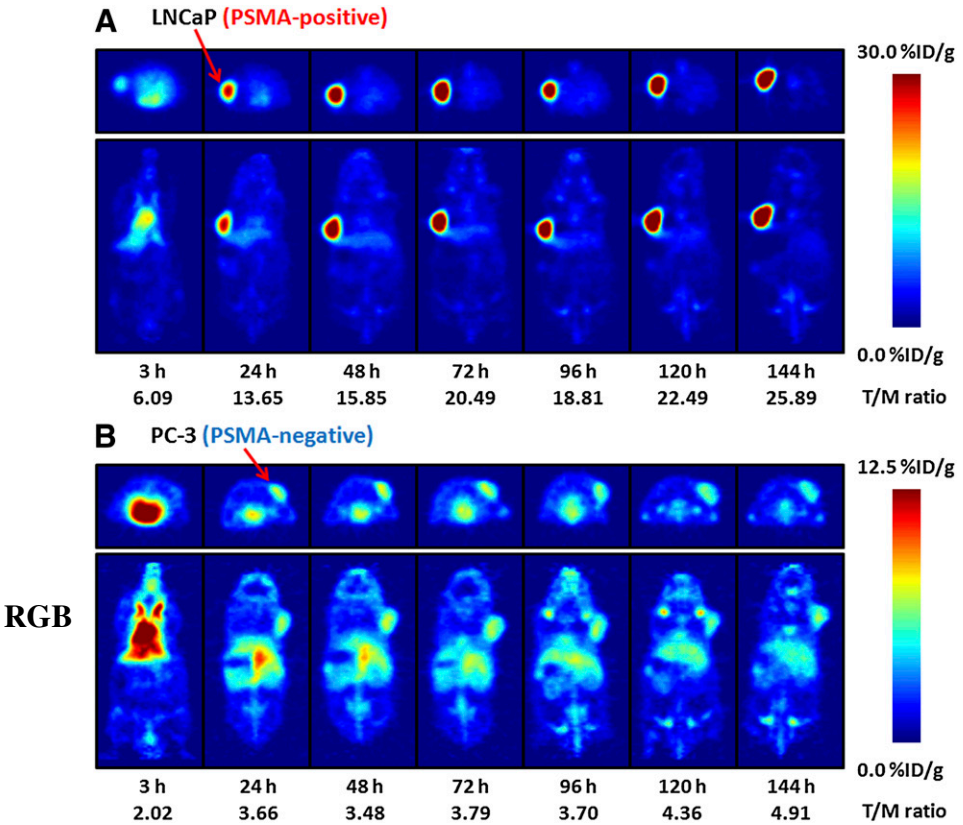

FIGURE 4. Temporal immunoPET images of ^{89}Zr-DFO-J591 (10.9–11.3 MBq [295–305 μCi], 60–62 μg of mAb, in 200 μL of sterile saline) recorded in LNCaP tumor–bearing (PSMA-positive, left shoulder) (A) and PC-3 tumor–bearing (PSMA-negative, right shoulder) (B) mice between 3 and 144 h after injection. Transverse and coronal planar images intersect center of tumors, and mean tumor-to-muscle ratios derived from volume-of-interest analysis of immunoPET images are given. Upper thresholds of immunoPET have been adjusted for visual clarity, as indicated by scale bars.

CONCLUSION

^{89}Zr-DFO-J591 has been prepared with a high RCP (>99%) and specific activity (181.7 ± 1.1 MBq/mg). In vitro stability studies demonstrated that functionalization of J591 with 3.9 ± 0.3 accessible DFO chelates per mAb and subsequent radiolabeling do not compromise the immunoreactivity, and radiolabeled immunoconjugate remains active for up to 7 d at 37°C. Biodistribution and immunoPET experiments indicated that ^{89}Zr-DFO-J591 shows high potential as a radiotracer for specific, noninvasive delineation of PSMA-positive PCs in vivo. Work toward the clinical translation of ^{89}Zr-DFO-J591 and other ^{89}Zr-labeled mAbs is under way.

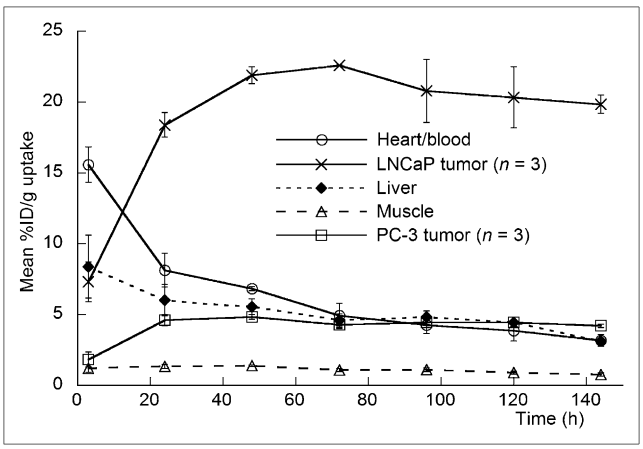

FIGURE 5. Time–activity curves derived by volume-of-interest analysis of immunoPET images showing mean %ID/g tissue uptake vs. time/h for ^{89}Zr-DFO-J591 radiotracer accumulation in mice bearing subcutaneous LNCaP (PSMA-positive) or PC-3 (PSMA-negative) tumors. Complete time–activity curve data for ^{89}Zr-DFO-J591 immunoPET imaging is given in supplemental materials (Supplemental Tables 9 and 10; Supplemental Figs. 11–13).

ACKNOWLEDGMENTS

We thank Drs. NagaVaraKishore Pillarsetty and Pat Zanzonico for informative discussions, Valerie M. Longo for assistance with the biodistribution experiments, Thomas Ku for advice with in vitro experiments, and Bradley Beattie for assistance with PET. We thank Professor Jennifer C. Green (Department of Chemistry, University of Oxford, United Kingdom) for access to computational facilities. We also thank the staff of the Radiochemistry/Cyclotron Core at the Memorial Sloan-Kettering Cancer Center (MSKCC). This study was funded in part by the Geoffrey Beene Cancer Research Center of Memorial Sloan-Kettering Cancer Center; the Office of Science (BER), U.S. Department of Energy (award DE-SC0002456); the Ludwig Center for Cancer Immunotherapy of the Sloan-Kettering Institute; and the Starr Cancer Consortium. Technical services provided by the MSKCC Small-Animal Imaging Core Facility were supported in part by NIH grants R24 CA83084 and P30 CA08748. Dr. Neil

Bander is the inventor on patents that are owned by Cornell Research Foundation (CRF) for the J591 antibody described in this manuscript. Dr. Neil Bander is a paid consultant to BZL Biologics, the company to which the patents were licensed by CRF for further research and development.

REFERENCES

1. Apolo AB, Pandit-Taskar N, Morris MJ. Novel tracers and their development for the imaging of metastatic prostate cancer. *J Nucl Med.* 2008;49:2031–2041.
2. Olson WC, Heston WDW, Rajasekaran AK. Clinical trials of cancer therapies targeting prostate-specific membrane antigen. *Rev Recent Clin Trials.* 2007;2:182–190.
3. Jhanwar YS, Divgi C. Current status of therapy of solid tumors. *J Nucl Med.* 2005;46(1 suppl):141S–150S.
4. Sokoloff RL, Norton KC, Gasior CL, Marker KM, Grauer LS. A dual-monoclonal sandwich assay for prostate-specific membrane antigen: levels in tissues, seminal fluid and urine. *Prostate.* 2000;43:150–157.
5. Manyak MJ. Indium-111 capromab pendetide in the management of recurrent prostate cancer. *Expert Rev Anticancer Ther.* 2008;8:175–181.
6. Morris MJ, Pandit-Taskar N, Divgi CR, et al. Phase I evaluation of J591 as a vascular targeting agent in progressive solid tumors. *Clin Cancer Res.* 2007;13:2707–2713.
7. Liu H, Moy P, Kim S, et al. Monoclonal antibodies to the extracellular domain of prostate-specific membrane antigen also react with tumor endothelium. *Cancer Res.* 1997;57:3629–3634.
8. Liu H, Rajasekaran AK, Moy P, et al. Constitutive and antibody-induced internalization of prostate-specific membrane antigen. *Cancer Res.* 1998; 58:4055–4060.
9. Smith-Jones PM, Vallabahajosula S, Goldsmith SJ, et al. *In vitro* characterization of radiolabeled monoclonal antibodies specific for the extracellular domain of prostate-specific membrane antigen. *Cancer Res.* 2000;60:5237–5243.
10. Smith-Jones PM, Vallabhajosula S, Navarro V, Bastidas D, Goldsmith SJ, Bander NH. Radiolabeled monoclonal antibodies specific to the extracellular domain of prostate-specific membrane antigen: preclinical studies in nude mice bearing LNCaP human prostate tumor. *J Nucl Med.* 2003;44:610–617.
11. McDevitt MR, Barendswaard E, Ma D, et al. An α-particle emitting antibody ([^{213}Bi]J591) for radioimmunotherapy of prostate cancer. *Cancer Res.* 2000;60:6095–6100.
12. Vallabhajosula S, Smith-Jones PM, Navarro V, Goldsmith SJ, Bander NH. Radioimmunotherapy of prostate cancer in human xenografts using monoclonal antibodies specific to prostate specific membrane antigen (PSMA): studies in nude mice. *Prostate.* 2004;58:145–155.
13. Vallabhajosula S, Kuji I, Hamacher KA, et al. Pharmacokinetics and biodistribution of ^{111}In- and ^{177}Lu-labeled J591 antibody specific for prostate-specific membrane antigen: prediction of ^{90}Y-J591 radiation dosimetry based on ^{111}In or ^{177}Lu? *J Nucl Med.* 2005;46:634–641.
14. Bander NH, Trabulsi EJ, Kostakoglu L, et al. Targeting metastatic prostate cancer with radiolabeled monoclonal antibody J591 to the extracellular domain of prostate specific membrane antigen. *J Urol.* 2003;170:1717–1721.
15. Vallabhajosula S, Goldsmith SJ, Hamacher KA, et al. Prediction of myelotoxicity based on bone marrow radiation-absorbed dose: radioimmunotherapy studies using ^{90}Y- and ^{177}Lu-labeled J591 antibodies specific for prostate-specific membrane antigen. *J Nucl Med.* 2005;46:850–858.
16. Vallabhajosula S, Goldsmith SJ, Kostakoglu L, Milowsky M, Nanus DM, Bander NH. Radioimmunotherapy of prostate cancer using ^{90}Y- and ^{177}Lu-labeled J591 monoclonal antibodies: effect of multiple treatments on myelotoxicity. *Clin Cancer Res.* 2005;11(19, suppl):7195s–7200s.
17. Bander NH, Milowsky MI, Nanus DM, Kostakoglu L, Vallabhajosula S, Goldsmith SJ. Phase I trial of ^{177}Lu-labeled J591, a monoclonal antibody to prostate-specific membrane antigen, in patients with androgen-independent prostate cancer. *J Clin Oncol.* 2005;23:4591–4601.
18. Milowsky MI, Nanus DM, Kostakoglu L, et al. Vascular targeted therapy with anti-prostate-specific membrane antigen monoclonal antibody J591 in advanced solid tumors. *J Clin Oncol.* 2007;25:540–547.
19. Pandit-Taskar N, O'Donoghue JA, Morris MJ, et al. Antibody mass escalation study in patients with castration-resistant prostate cancer using ^{111}In-J591: lesion detectability and dosimetric projections for ^{90}Y radioimmunotherapy. *J Nucl Med.* 2008;49:1066–1074.
20. McDevitt MR, Ma D, Lai LT, et al. Tumor therapy with targeted atomic nanogenerators. *Science.* 2001;294:1537–1540.
21. Frisch MJ, Trucks GW, Schlegel HB, et al. *Gaussian 03, Revision-C.02*. Wallingford, CT: Gaussian, Inc.; 2004.
22. Holland JP, Caldas-Lopes E, Divilov V, et al. Measuring the pharmacokinetic effects of a novel Hsp90 inhibitor on HER2/*neu* expression in mice using ^{89}Zr-DFO-trastuzumab. *PLoS ONE.* 2010;5:e8859.
23. Verel I, Visser GWM, Boellaard R, Stigter-van Walsum M, Snow GB, van Dongen GAMS. ^{89}Zr immuno-PET: comprehensive procedures for the production of ^{89}Zr-labeled monoclonal antibodies. *J Nucl Med.* 2003;44:1271–1281.
24. Holland JP, Sheh Y, Lewis JS. Standardized methods for the production of high specific-activity zirconium-89. *Nucl Med Biol.* 2009;36:729–739.
25. Kim JS, Lee JS, Im KC, et al. Performance measurement of the microPET Focus 120 scanner. *J Nucl Med.* 2007;48:1527–1535.
26. Verel I, Visser GWM, Boellaard R, et al. Quantitative ^{89}Zr immuno-PET for in vivo scouting of ^{90}Y-labeled monoclonal antibodies in xenograft-bearing nude mice. *J Nucl Med.* 2003;44:1663–1670.
27. Perk LR, Visser OJ, Stigter-van Walsum M, et al. Preparation and evaluation of ^{89}Zr-Zevalin for monitoring of ^{90}Y-Zevalin biodistribution with positron emission tomography. *Eur J Nucl Med Mol Imaging.* 2006;33:1337–1345.
28. Börjesson PKE, Jauw YWS, Boellaard R, et al. Performance of immuno-positron emission tomography with zirconium-89-labeled chimeric monoclonal antibody U36 in the detection of lymph node metastases in head and neck cancer patients. *Clin Cancer Res.* 2006;12:2133–2140.
29. Borjesson PKE, Jauw YWS, de Bree R, et al. Radiation dosimetry of ^{89}Zr-labeled chimeric monoclonal antibody U36 as used for immuno-PET in head and neck cancer patients. *J Nucl Med.* 2009;50:1828–1836.
30. Perk LR, Stigter-van Walsum M, Visser GWM, et al. Quantitative PET imaging of Met-expressing human cancer xenografts with ^{89}Zr-labelled monoclonal antibody DN30. *Eur J Nucl Med Mol Imaging.* 2008;35: 1857–1867.
31. Aerts HJWL, Dubois L, Perk L, et al. Disparity between in vivo EGFR expression and ^{89}Zr-labeled cetuximab uptake assessed with PET. *J Nucl Med.* 2009;50:123–131.
32. Dijkers ECF, Kosterink JGW, Rademaker AP, et al. Development and characterization of clinical-grade ^{89}Zr-trastuzumab for HER2/neu immunoPET imaging. *J Nucl Med.* 2009;50:974–981.
33. Lindmo T, Boven E, Cuttitta F, Fedorko J, Bunn PA Jr. Determination of the immunoreactive fraction of radiolabeled monoclonal antibodies by linear extrapolation to binding at infinite antigen excess. *J Immunol Methods.* 1984;72:77–89.
34. Meijs WE, Herscheid JDM, Haisma HJ, Pinedo HM. Evaluation of desferal as a bifunctional chelating agent for labeling antibodies with Zr-89. *Int J Rad Appl Instrum A.* 1992;43:1443–1447.
35. Meijs WE, Haisma HJ, Klok RP, et al. Zirconium-labeled monoclonal antibodies and their distribution in tumor-bearing nude mice. *J Nucl Med.* 1997;38:112–118.
36. Nagengast WB, de Vries EG, Hospers GA, et al. *In vivo* VEGF imaging with radiolabeled bevacizumab in a human ovarian tumor xenograft. *J Nucl Med.* 2007;48:1313–1319.

jnm076174-pm ■ 7/12/10